Available online at www.sciencedirect.com
ScienceDirect
Polymer 48 (2007) 4226–4234
polymer
www.elsevier.com/locate/polymer

Interplay of crystallization and liquid–liquid phase separation in polyolefin blends: A thermal history dependence study

Katsumi Shimizu [a,*], Howard Wang [b,**], Go Matsuba [c], Zhigang Wang [d], Hongdoo Kim [e], Weiqun Peng [f], Charles C. Han [g]

[a] *Advanced Protein Crystallography Research Group, RIKEN Harima Institute, 1-1-1 Kouto, Sayo-chou, Sayo-gun, Hyogo 679-5148, Japan*
[b] *Department of Mechanical Engineering, Binghamton University, SUNY, Binghamton, NY 13902, United States*
[c] *Institute for Chemical Research, Kyoto University, Gokasho, Uji, Kyoto 611-0011, Japan*
[d] *CAS Key Laboratory of Engineering Plastics, Joint Laboratory of Polymer Science and Materials, Institute of Chemistry, The Chinese Academy of Sciences, Beijing 100080, PR China*
[e] *Department of Chemistry, Kyung Hee University, Kyungkido 449-701, South Korea*
[f] *Department of Physics, George Washington University, Washington DC, United States*
[g] *State Key Laboratory of Polymer Physics and Chemistry, Joint Laboratory of Polymer Science and Materials, Institute of Chemistry, The Chinese Academy of Sciences, Beijing 100080, PR China*

Received 21 January 2007; received in revised form 4 May 2007; accepted 8 May 2007
Available online 13 May 2007

Abstract

The kinetic interplay between crystallization and liquid–liquid phase separation (LLPS) in random copolymer blends of poly(ethylene-*ran*-hexene) (PEH) and poly(ethylene-*ran*-butene) (PEB) has been studied using optical microscopy. Morphologies of blends gone through three different thermal histories are compared: (1) single-quench (SQ), a homogeneous melt quickly cooled to isothermal crystallization temperatures (T_{cry}), (2) double-quench (DQ), a homogeneous melt quickly cooled to an intermediate temperature (T_{lps}) between binodal and equilibrium melting temperature (T_m^0) and stored for a period of time and then cooled to T_{cry}, and (3) cyclic-quench (CQ), a homogeneous melt quickly cooled to T_{lps} and stored for a period of time, then gone through four cycles of crystallization and remelting. Comparing DQ morphologies to SQ ones, both crystal growth rate and nucleation density in the former are affected by prior LLPS. A scaling argument has been provided to partially account for the observed phenomena. In CQ, characteristic lengths of secondary features induced by crystallization depend strongly on the overall PEH composition, whereas are insensitive to temperature cycling. The contrast of large domains becomes more prominent upon cyclic crystallization and remelting. On the other hand, primary LLPS domains coarsen with CQ while loosing the contrast.

Keywords: Polyolefins; Crystallization; Phase separation

1. Introduction

The morphology of polyolefin blends is often due to the interplay between crystallization and liquid–liquid phase separation (LLPS), the two widely studied and common phase transitions in polymers [1–5]. A fundamental understanding of such interplay remains a big challenge. An in-depth study would require both an accurate account of the equilibrium phase diagram and careful characterization of the kinetics of the non-equilibrium phase-transition processes. Dynamical behaviors of crystallization and LLPS are fundamentally different. While crystallization develops via the activated process of nucleation, LLPS below spinodal line proceeds via the emergence and subsequent growth of infinitesimal long-wavelength fluctuations. In this paper, we explore the

* Corresponding author. Tel.: +81 791 58 0802x7845; fax: +81 791 58 2917.
** Corresponding author.
E-mail addresses: kshimizu@spring8.or.jp (K. Shimizu), wangh@binghamton.edu (H. Wang).

0032-3861/$ - see front matter © 2007 Elsevier Ltd. All rights reserved.
doi:10.1016/j.polymer.2007.05.005

competition of the two phase-transition processes by moving the system through thermodynamic states via different paths of non-equilibrium quenching processes. Although studies on crystallization in polymer blends are abundant, some of them are limited for illustrating both the thermodynamic and kinetic interplays. For example, a previous study on kinetics competition used immiscible blends of polypropylene and ethylene–propylene random copolymer [6,7], which have uncertainty of the thermodynamic condition; in another study, poly(ε-caprolactone) and polystyrene blend [8–10] have well-defined phase diagram, but large dynamic contrast between two components allows for observation of kinetics in limited parameter space.

Burghardt reported the first explicit theoretical calculation of the phase diagram for polymer blends that exhibit both LLPS and crystallization [11]. In a simple binary blend possessing an upper critical solution temperature (UCST) in the melt, if the equilibrium melting temperature (T_m^0) is below the UCST, it is possible to have temperature/composition regimes for LLPS to occur prior to crystallization or simultaneous LLPS and crystallization. In our previous studies, we have identified a model metallocene polyolefin pair with UCST above T_m^0 with well-defined phase-transition diagrams [12,13], and studied various thermodynamic and kinetics aspects of the model blend [14–25]. In this article, we focus on comparing the morphology development in polyolefin blends due to the interplay between the LLPS and crystallization in three different thermal quench sequences including (1) single-quench (SQ) from a homogeneous melt to simultaneous crystallization and LLPS, (2) double-quench (DQ) initially to an intermediate temperature for LLPS then to crystallization temperature, and (3) cyclic-quench (CQ) for cycles of crystallization and remelting.

2. Experimental

The polymers used in the present study are statistical copolymers of poly(ethylene-*ran*-hexene) (PEH) and poly(ethylene-*ran*-butene) (PEB), synthesized using metallocene catalysts. The characteristics of the two polymers, including mass-averaged molecular mass (M_w), mass density (ρ_m), side chain density (ρ_b), as well as the melting temperature (T_m) are listed in Table 1. These polymers were synthesized by metallocene catalysts and have a relatively narrow polydispersity (~2) and branching density distribution. Mixtures of various compositions were prepared by co-precipitating from a hot xylene solution (ca. 100 °C) with a polymer mass fraction of ca. 3% into methanol at room temperature. After filtering, the polymers were dried in air for 24 h and further dried in vacuum oven at room temperature for 3 days. Here, blends with 60%, 50%, 40% and 30% mass fraction of PEH, denoted as H60, H50, H40 and H30, respectively, were investigated. The blends were pressed between two cover glasses at 160 °C to make film of ca. 50 μm and then quenched to room temperature in air. The pressed polymer was surrounded with silicon oil and the cover glasses were sealed with epoxy resin to avoid the thermal degradation of the polymer.

Table 1
Characteristics of PEH and PEB

	PEH	PEB
Mass-averaged molecular mass: M_w (Kg/mol)	112	70
Mass density: ρ_m (g/cm^3)	0.922	0.875
Branching density[a]: ρ_b (per 1000C)	9	77
Melting temperature[b]: T_m (°C)	120	48

[a] ρ_b, in unit of per 1000 backbone carbon atoms.
[b] The differential scanning calorimetry was carried out for deciding the melting temperature of PEH and PEB. Details of the thermal history are explained in reference [13].

The phase diagram of PEH/PEB blend has been determined previously, as shown in Fig. 1 [12,13]. The LLPS phase boundary possesses a UCST at $T_c = 146$ °C at the critical composition $\phi_c = 0.44$ in the melt, and follows Flory–Huggins theory for binary polymer mixtures. The T_m^0 of blends decreases with increasing PEB concentration in the one-phase regime, whereas T_m^0 remains relatively constant in the two-phase regime, at ca. 127 °C.

The temperature sequences were programmed based on the phase diagram, as shown in Fig. 2. In SQ [Fig. 2a], the blends were first annealed at 160 °C for $t_{hom} = 5$ min to remove the previous thermal history and then quenched to a lower temperature, T_{cry}, for isothermal crystallization, or T_{lps} for LLPS. In DQ [Fig. 2b], blends were annealed at 160 °C for 5 min and then quenched to an intermediate temperature between T_m^0 and binodal temperature, T_{lps}, and stored for a period of ($t_{lps} - t_{hom}$), after which blends were further quenched to T_{cry} for crystallization. In CQ [Fig. 2c], blends were annealed at 160 °C for 5 min and quenched to T_{lps}, followed by four cycles of cooling and heating to allow for repeated crystallization and remelting. The

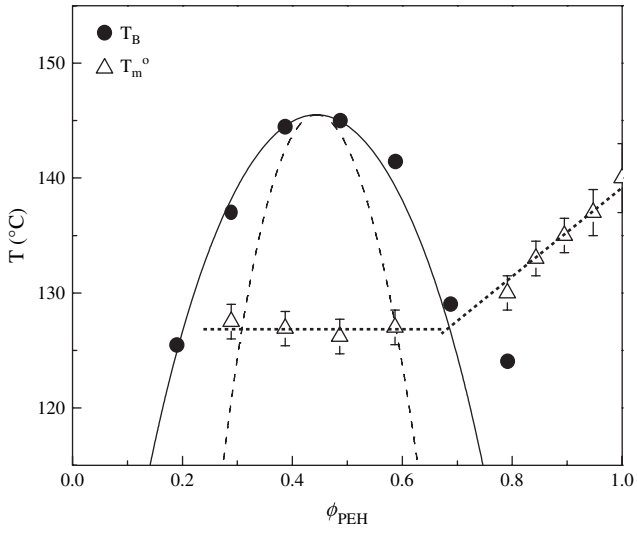

Fig. 1. Phase diagram of PEH/PEB blend. The phase diagram shows an upper critical solution temperature of $T_{cry} = 146$ °C at the critical composition $\phi_{cri} = 0.44$. The binodal temperature and equilibrium melting temperature have been clarified with light scattering experiment and differential scanning calorimetry. The solid and dashed curves represent binodal and spinodal boundaries, respectively. The dotted line through the equilibrium melting temperature is guide to eye.

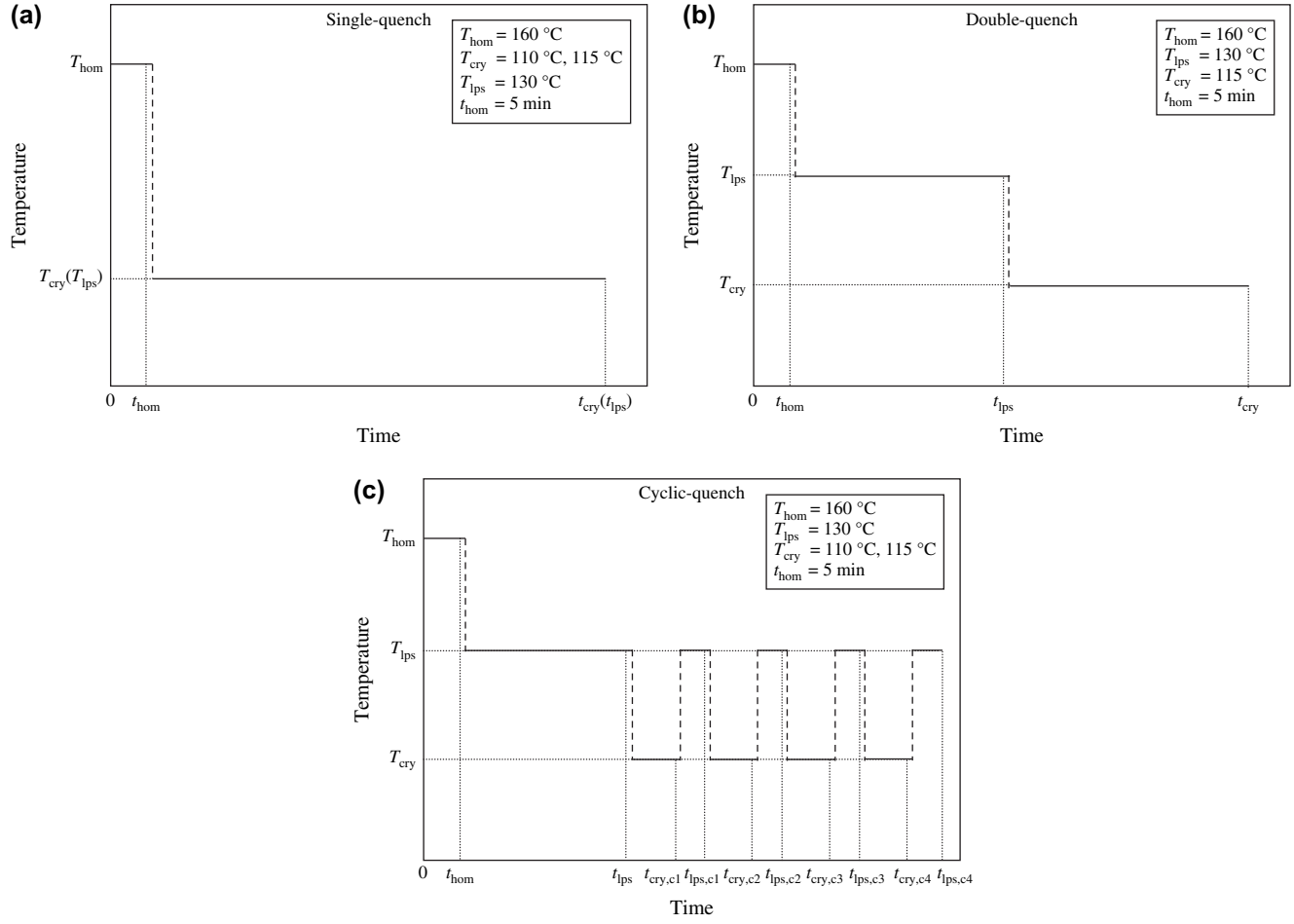

Fig. 2. Thermal histories of (a) single-quench, (b) double-quench and (c) cyclic-quench conditions. The solid lines represent the temperature processes for isothermal duration. The heating and cooling processes are shown by vertical dashed lines. The homogenizing temperature above equilibrium melting temperature, liquid–liquid phase-separation temperature and crystallization temperature are shown by T_{hom}, T_{lps} and T_{cry}, respectively. The accumulated experimental time for homogenizing, liquid–liquid phase separation, and crystallization are shown by t_{hom}, t_{lps} and t_{cry}, respectively. In cyclic-quench condition, the order of cyclic-quench processes are distinguished by the subscript ci ($i = 1$, 2, 3 and 4) and the accumulated experimental time for liquid–liquid phase separation and crystallization are shown by $t_{lps,ci}$ and $t_{cry,ci}$, respectively.

temperature stability of the hot-stage was within ±0.1 °C. The blend morphology was recorded using a Leitz optical microscope with a Sony CCD video camera module (XC-77). The size of the spherulites was measured by averaging the height and width of a well-defined representative spherulite. The characteristic length of LLPS, l_m, was characterized by 2D fast-Fourier transform (2D-FFT) of optical microscope images. The FFT images were then radially averaged to yield 1D intensity profile. The characteristic length is defined as $l_m \sim 2\pi/q_m$, where q_m is the peak wave vector.

3. Results and discussion

To compare with the morphology developed in the two-phase region, we first present the representative crystallization and LLPS morphologies observed in SQ and CQ conditions in H50 near the critical composition (Fig. 3). According to the phase diagram, the binodal temperature, T_B, and equilibrium melting temperature, T_m^0, for H50 are ca. 144 and ca. 127 °C, respectively.

In SQ at $T_{cry} = 115$ °C, crystallization has been observed (Fig. 3a). The brighter features in the micrograph are spherulites, which were confirmed in a previous study [14]. The spherulites observed at 115 °C are composed of PEH component because of the lower melting temperature (48 °C) of PEB (Table 1). If the final temperature in SQ is 130 °C, between T_B and T_m^0 for H50, interconnected bicontinuous morphology of LLPS is observed (Fig. 3b). The distinction of the two bicontinuous phases has been investigated in our previous paper and the darker and lighter matrices in the tube-like morphology correspond to the PEH- and PEB-rich phases, respectively [14,15]. In CQ conditions, crystallized morphology at $T_{cry} = 110$ °C shows fine tube-like features superimposed by large scale undulations (Fig. 3c), which persist while the blend is brought to melting at 130 °C (Fig. 3d). Note that the contrast of the domain is reversed comparing Fig. 3c and d: the lighter regions correspond to PEH-rich crystals at 110 °C, while they are PEB-rich phases at 130 °C. Details of the experiment including time evolution of the morphology and composition dependence will be given later.

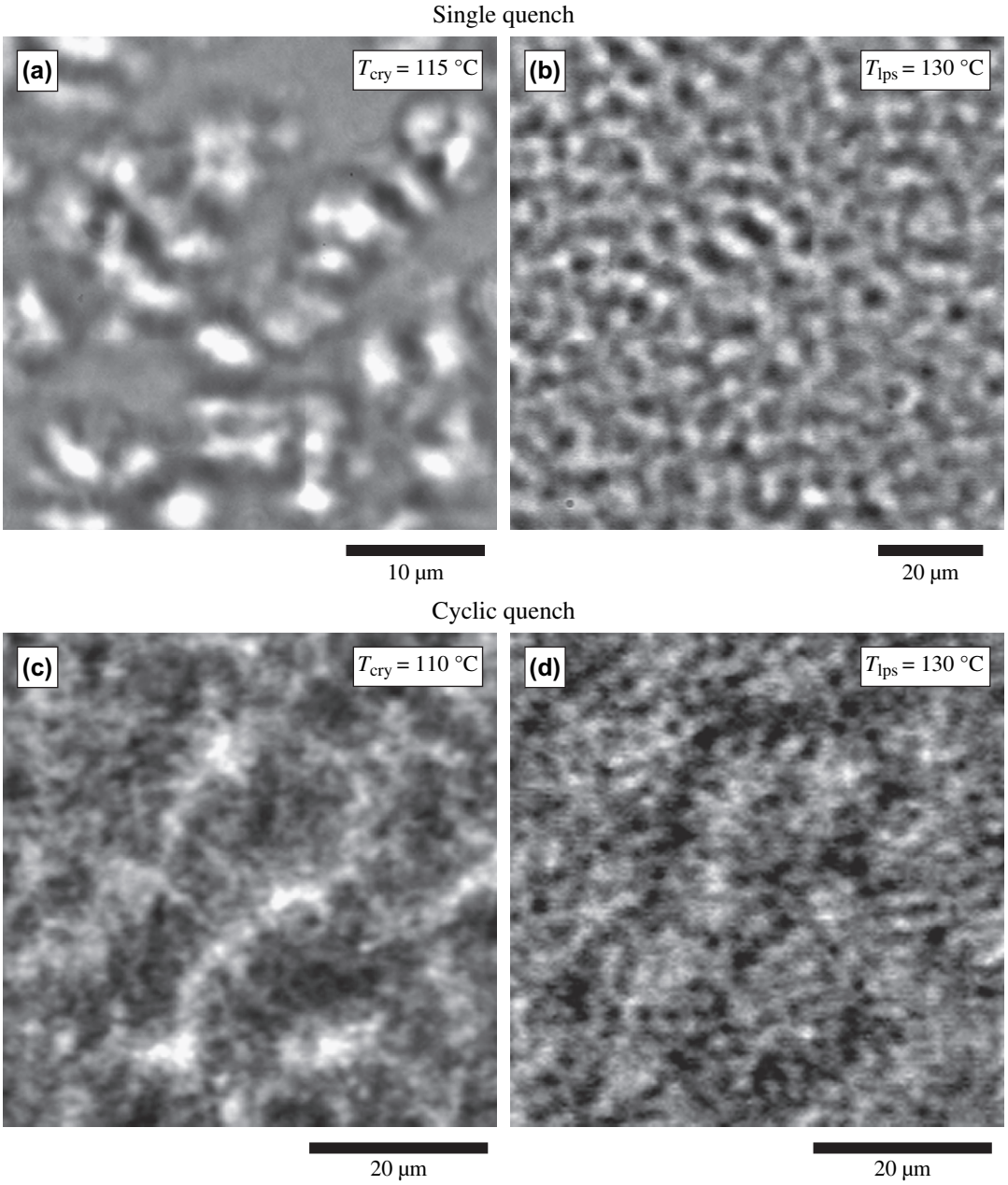

Fig. 3. Distinction of phase structures in H50 developed by the single-quench ((a) and (b)) and cyclic-quench ((c) and (d)) conditions for: (a) $T_{cry} = 115\ ^{\circ}C$, $t_{cry} = 106$ min, (b) $T_{lps} = 130\ ^{\circ}C$, $t_{lps} = 1465$ min, (c) $T_{cry} = 115\ ^{\circ}C$, $t_{cry,c4} = 331$ min and (d) $T_{lps} = 130\ ^{\circ}C$, $t_{lps,c4} = 337$ min. The scale bar for each image is denoted at the bottom right.

Fig. 4 compares bright-field optical micrographs of H50 at (a) $T_{cry} = 115\ ^{\circ}C$ in SQ, for $t_{cry} - t_{hom} = 15$ min, and (b–d) in DQ for various LLPS times: (b) $t_{lps} - t_{hom} = 133$ min, $t_{cry} - t_{lps} = 5$ min, (c) $t_{lps} - t_{hom} = 257$ min, $t_{cry} - t_{lps} = 5$ min, and (d) $t_{lps} - t_{hom} = 493$ min, $t_{cry} - t_{lps} = 5$ min. In all experiments, spherulites have been observed to grow with time. Crystallization kinetics and nucleation density could be measured from micrographs. The time evolution of the average size of spherulites, D_{sph}, for H50 is quantified in SQ and DQ as shown in Fig. 5. In both cases, D_{sph} grows linearly with time at the early time and saturates in later times. The crystallization growth rate, G, was determined by fitting the initial linear growth region shown as the line through the symbols. The inset in Fig. 5 shows LLPS time, $t_{lps} - t_{hom}$, dependence of G at $T_{lps} = 130\ ^{\circ}C$ and $T_{cry} = 115\ ^{\circ}C$ for H50. The data at $t_{lps} - t_{hom} = 0$ correspond to that in SQ. G of DQ is generally greater than that in SQ. However, G depresses at $t_{lps} - t_{hom} = 257$ min. The nucleation density of crystallite, ρ, has been quantified as a function of LLPS time, $t_{lps} - t_{hom}$ (Fig. 6). ρ in DQ is generally smaller than that in SQ except for $t_{lps} - t_{hom} = 257$ min, after which ρ is approximately eight times higher.

There are many interesting features in the crystallization growth rate and nucleation density in SQ and DQ experiments. For example, both nucleation density and crystallization

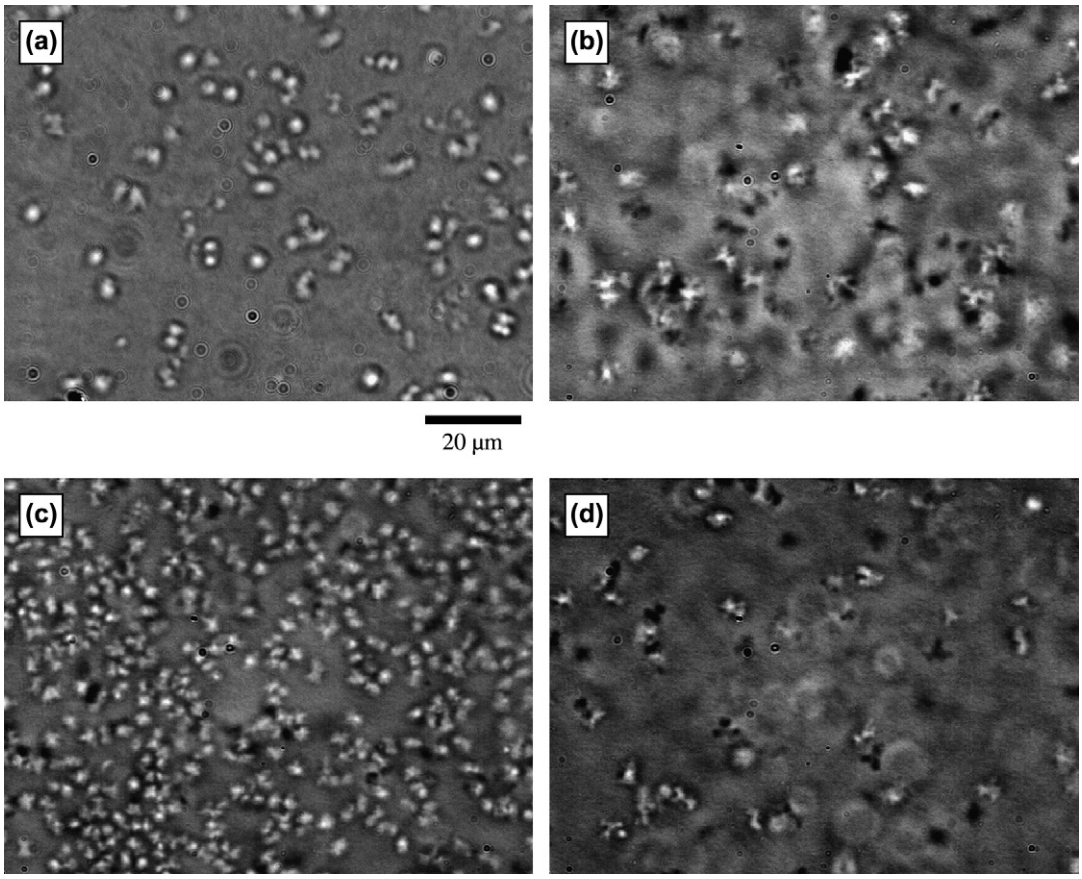

Fig. 4. Bright-field optical micrographs of H50 at $T_{cry} = 115\ ^{\circ}C$ for single-quench condition: (a) $t_{cry} - t_{hom} = 15$ min and double-quench condition, (b) $t_{lps} - t_{hom} = 133$ min, $t_{cry} - t_{lps} = 5$ min, (c) $t_{lps} - t_{hom} = 257$ min, $t_{cry} - t_{lps} = 5$ min, and (d) $t_{lps} - t_{hom} = 493$ min, $t_{cry} - t_{lps} = 5$ min. The scale bar is applicable for all images and represents 20 μm.

kinetics in DQ are different from those in SQ, but the variations are not monotonic. The observed phenomena could be understood based on a physical picture of interplay between LLPS and crystallization. In a phase-separated blend, crystals mostly start to grow in the PEH-rich phase because of the abundant crystallizable PEH component. For interconnected domain structures developed due to spinodal decomposition, a characteristic length scale L is used to describe the domain pattern. The domain size L depends on ε, the strength of

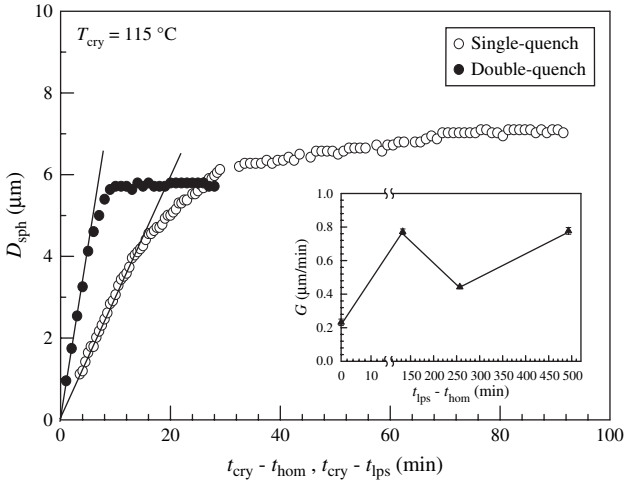

Fig. 5. Time evolution of the average spherulite size, D_{sph}, for H50 in single-quench condition and double-quench condition ($t_{lps} - t_{hom} = 125$ min). D_{sph} for these quench cases is shown as a function of $t_{cry} - t_{hom}$ for single-quench condition and $t_{cry} - t_{lps}$ for double-quench condition. The slope of solid line represents the crystallization growth rate, G. The inset shows isothermal liquid–liquid phase-separation time, $t_{lps} - t_{hom}$, dependence of G. G at $t_{lps} - t_{hom} = 0$ min corresponds to that in single-quench condition.

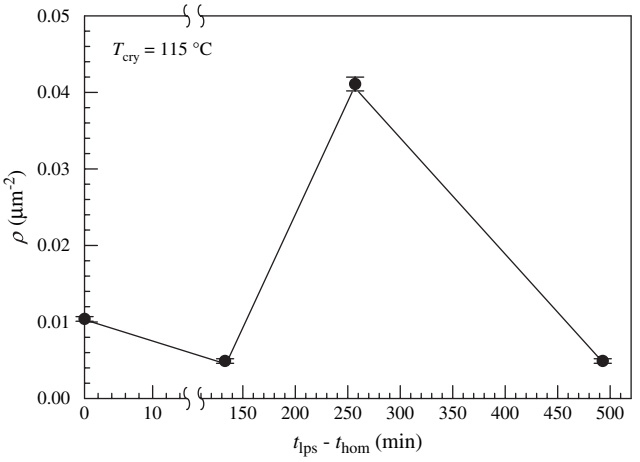

Fig. 6. Isothermal LLPS time, $t_{lps} - t_{hom}$, dependence of the nucleation density, ρ, of H50 for single-quench and double-quench conditions. ρ at $t_{lps} - t_{hom} = 0$ min corresponds to that in single-quench condition.

disorder and t, the time elapsed since quenching. We assume the following scaling form for $L(\varepsilon,t)$ [26]:

$$L(\varepsilon,t) = \varepsilon^{-\alpha} F(t\varepsilon^{\gamma}) \quad (1)$$

The physical significance of exponents α and γ can be understood as follows. When ε is fixed and non-zero, the scaling function $F(t\varepsilon^{\gamma})$ needs to approach a constant value as $t \to \infty$. Therefore the exponent α represents the scaling of domain size with respect to disorder strength *at equilibrium*. On the other hand, in the limit of zero disorder $(\varepsilon \to 0)$, $L(\varepsilon,t)$ should approach the well-known power law t^{φ}, with the exponent φ consistent with a value of 1/3. This requires that $F(t\varepsilon^{\gamma}) \sim (t\varepsilon^{\gamma})^{\alpha/\gamma}$ as $t\varepsilon^{\gamma} \to 0$. As a result, γ is determined by the static exponent α and dynamical exponent φ, $\gamma = \alpha/\varphi$. As $t\varepsilon^{\alpha/\varphi} \to 0$ for regimes under study while the behavior of the system changes as $t_{\mathrm{lps}} - t_{\mathrm{hom}}$, the experimentally relevant scaling behavior for domain size is simply $L \propto t^{\varphi}$. This scaling behavior is used to understand the nucleation in phase separating blend.

Two factors are important in crystallization, the appearance of nuclei and the transport of PEH for growing nuclei. Most nucleation events develop at the interface between the PEH-rich phase and PEB-rich phase [27,28], therefore the nucleation density is roughly proportional to the area of the domain interface. Domain patterns being a fractal structure, assume that the interfacial area $S \propto L^{-\sigma} \propto t^{-\varphi\sigma}$, where $2 < \sigma < 3$. Therefore, when $t_{\mathrm{lps}} - t_{\mathrm{hom}}$ is small, the domain size is small, the interfacial area is large, and the nucleation probability is larger. On the other hand, assuming that the growth of nuclei is mainly due to diffusion of PEH within PEH-rich domains, the diffusion process is slowed down because it is restricted into a quasi one-dimensional tube of cross-section L^2 when domain size is small. Therefore, the growth rate and the size of a nucleus after a certain time scales with L^2. This results in significant difficulty in the growth of nuclei when domain size is small. What is observed in experiments, ρ, is the density of nuclei that are above certain minimal size after a fixed amount of time $t_{\mathrm{cry}} - t_{\mathrm{lps}}$. Taken together, the above argument proposes that $\rho \propto L^{2-\sigma} \propto (t_{\mathrm{lps}} - t_{\mathrm{hom}})^{(2-\sigma)\varphi}$. This scaling relation explains the decrease of nuclei density for $t_{\mathrm{lps}} - t_{\mathrm{hom}}$ greater than 257 min. At shorter $t_{\mathrm{lps}} - t_{\mathrm{hom}}$, the average size of nuclei is too small to be observed, only stochastic fluctuations above the sensitivity threshold are captured, to which the above scaling arguments do not apply. The scaling argument is not applicable for very short period after the second quench because the assumption that the growth of the nuclei happens through the quasi one-dimensional channels in the PEH-rich phase is no longer true.

The morphologies induced by the kinetic competition between crystallization and LLPS were further investigated by CQ experiment. Fig. 7 shows the phase-contrast optical micrographs of H50 at (a) $t_{\mathrm{lps}} - t_{\mathrm{hom}} = 0$ min, (b) $t_{\mathrm{lps}} - t_{\mathrm{hom}} = 242$ min, (c) $t_{\mathrm{lps,c1}} - t_{\mathrm{hom}} = 265$ min, (d) $t_{\mathrm{lps,c2}} - t_{\mathrm{hom}} = 286$ min, (e) $t_{\mathrm{lps,c3}} - t_{\mathrm{hom}} = 310$ min, (f) $t_{\mathrm{lps,c4}} - t_{\mathrm{hom}} = 332$ min. The inset of each micrograph corresponds to 2D-FFT image. After annealing for $t_{\mathrm{lps}} - t_{\mathrm{hom}} = 242$ min at $T_{\mathrm{lps}} = 130\ ^{\circ}\mathrm{C}$, interconnected bicontinuous morphology is observed (Fig. 7b). The emergence of the spinodal-ring is evident in the corresponding 2D-FFT image. Subsequently, the sample was quenched to $T_{\mathrm{cry}} = 110\ ^{\circ}\mathrm{C}$ and stored for approximately 20 min for crystallization, and then heated up to 130 °C. After one cycle of crystallization and remelting, large secondary domains are seen to superimpose on the original bicontinuous tube structures (Fig. 7c). Upon additional cyclic crystallization and remelting at T_{cry} and T_{lps}, respectively, the contrast of large scale domains enhances, while the length scale of small features coarsens (Fig. 7d–f).

The 2D-FFT intensities are radially averaged to yield the time evolution of the 1D intensity spectra as shown in Fig. 8. After annealing at $T_{\mathrm{lps}} = 130\ ^{\circ}\mathrm{C}$ for $t_{\mathrm{lps}} - t_{\mathrm{hom}} = 242$ min, a diffuse peak due to the interconnected bicontinuous structure appears at approximately $q_{\mathrm{m}} \sim 2.5\ \mu\mathrm{m}^{-1}$, corresponding to a characteristic length scale of ca. 2.5 μm. The peak shifts to $q_{\mathrm{m}} \sim 1.8\ \mu\mathrm{m}^{-1}$ after four CQs, indicating domain coarsening to a characteristic length of ca. 3.5 μm. On the other hand, a low-q peak at $\sim 0.3\ \mu\mathrm{m}^{-1}$ appears after the first CQ, corresponding to a characteristic length of ca. 20 μm for large domains induced by crystallization. The peak remains constant in position but becomes more prominent upon cyclic crystallizing and remelting.

CQ experiments were carried out at various blend compositions at the same $T_{\mathrm{lps}} = 130\ ^{\circ}\mathrm{C}$ and $T_{\mathrm{cry}} = 110\ ^{\circ}\mathrm{C}$. Fig. 9 shows the phase-contrast optical micrographs of H30 after (a) $t_{\mathrm{lps}} = 246$ min, (b) $t_{\mathrm{cry,c4}} = 346$ min, (c) $t_{\mathrm{lps,c4}} = 357$ min, of H40 after (d) $t_{\mathrm{lps}} = 259$ min, (e) $t_{\mathrm{cry,c4}} = 352$ min, (f) $t_{\mathrm{lps,c4}} = 361$ min, of H50 after (g) $t_{\mathrm{lps}} = 247$ min (h) $t_{\mathrm{cry,c4}} = 331$ min (i) $t_{\mathrm{lps,c4}} = 337$ min, and of H60 after (j) $t_{\mathrm{lps}} = 234$ min, (k) $t_{\mathrm{cry,c4}} = 315$ min, (l) $t_{\mathrm{lps,c4}} = 318$ min. After 240 min at 130 °C, bicontinuous LLPS morphology has been observed in (d) H40, (g) H50, and (j) H60. The features in H40 and H50 appear to be larger than that in H60 because of deeper quenches and larger driving force for LLPS. In H30, the vague phase-separation morphology is attributed to its composition near the spinodal phase boundary therefore slow LLPS kinetics. These observations are consistent with our previous morphological studies [14–18]. After four cycles of crystallization and remelting, large domains appear at all compositions, where brighter features correspond to PEH crystals. The length scale of large domains increases with PEH compositions, as shown in Fig. 9b, e, h and k. The contrast is reversed when the blends are brought to melting at 130 °C, while the fine tube-like textures resemble those before cyclic crystallization and melting (e.g. Fig. 9g vs. i for H50).

The characteristic length scale, l_{m}, of the large domains developed during CQ was calculated as $l_{\mathrm{m}} = 2\pi/q_{\mathrm{m}}$, where the q_{m} is the scattering vector of the low-q maximum intensity in 1D FFT spectra. Fig. 10 shows the variation of l_{m} in H30, H40 and H50 with the quench cycle, which increases with composition and is insensitive to cycles. Due to its large value, the l_{m} cannot be reliably determined for H60.

The development of large secondary domains observed in the CQ is due to the interplay between crystallization and phase separation. Upon the first quench from $T_{\mathrm{lps}} = 130\ ^{\circ}\mathrm{C}$ to $T_{\mathrm{cry}} = 110\ ^{\circ}\mathrm{C}$, crystals grow initially in PEH-rich phase until they are slowed at phase boundaries. However, crystals are able to grow through the phase boundary and penetrate

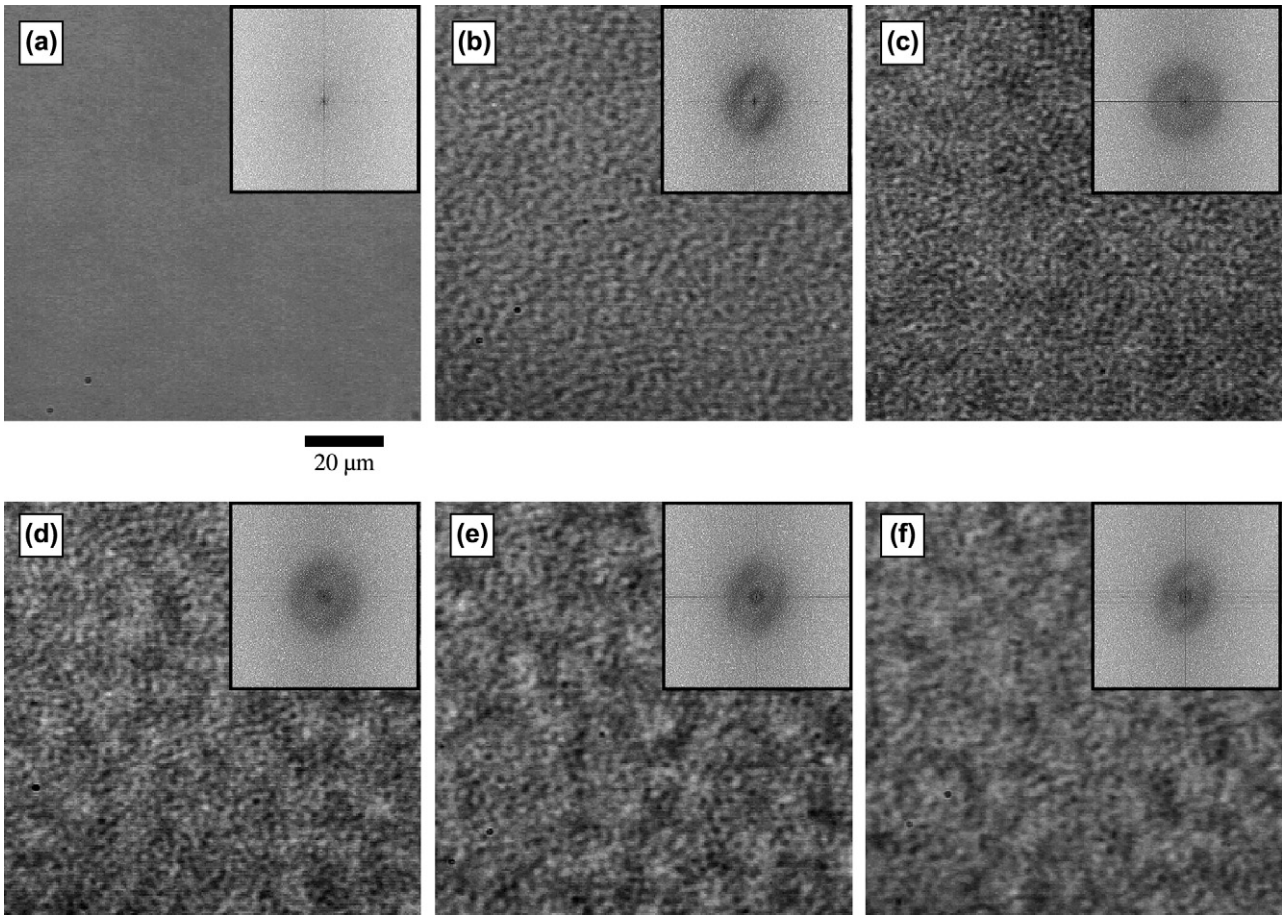

Fig. 7. Phase-contrast optical micrographs of H50 for cyclic-quench condition ($T_{lps} = 130$ °C, $T_{cry} = 110$ °C) for: (a) $t_{lps} - t_{hom} = 0$ min, (b) $t_{lps} - t_{hom} = 242$ min, (c) $t_{lps,c1} - t_{hom} = 265$ min, (d) $t_{lps,c2} - t_{hom} = 286$ min, (e) $t_{lps,c3} - t_{hom} = 310$ min, (f) $t_{lps,c4} - t_{hom} = 332$ min. The large secondary structure is formed through the cyclic crystallization and melting. The scale bar is applicable for all images and represents 20 μm.

into the PEB-rich phase due to the large driving force for crystallization. Although the LLPS tube structure is not destroyed, PEH-rich components accumulate through crystal growth, whereas non-crystallizable components rich in PEB

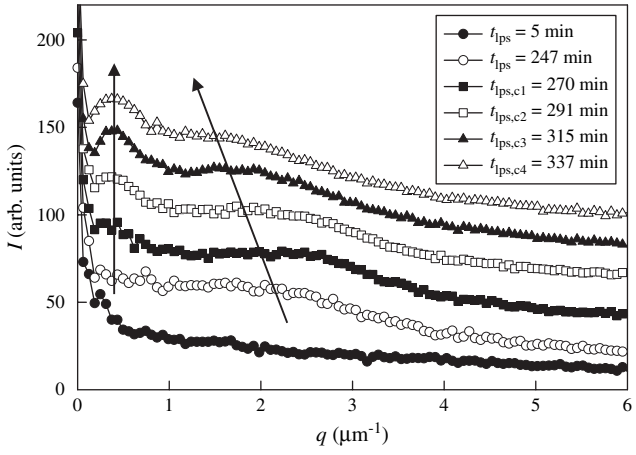

Fig. 8. Time evolution of the radially averaged 1D scattering profiles for H50 in cyclic-quench condition. The broad peak due to the coarsening of the interconnected bicontinuous structure is evident in the higher q region ($\sim$2.5 μm^{-1}), whereas another peak in the lower q region ($\sim$0.3 μm^{-1}) emerges through the cyclic crystallizing and melting.

are expelled from crystals, causing the development of the composition heterogeneity over a scale much large than the characteristic length scale of LLPS. The ''purified'' PEH-rich chains accumulate to form boundaries of large domains upon remelting. Little morphology change would be expected in melt because of the small interfacial tension and large viscosity. In subsequent recrystallization, the very crystallizable components at large domain boundaries crystallize to freeze the framework, preventing the coarsening of large domains with CQ; further segregation of crystallizable chains only enhances the contrast. On the contrary, repeated crystallization across the LLPS phase boundaries and remelting assist the coarsening of tube morphology while smearing its contrast.

4. Conclusion

The kinetic interplay between crystallization and LLPS and resulting morphology in statistical copolymer blends of PEH and PEB has been studied using optical microscopy. Morphologies of blends gone through thermal histories of single-quench, double-quench, and cyclic-quench have been observed. Comparing DQ morphologies to SQ ones, both crystal growth rate and nucleation density in the former are affected by prior LLPS. A scaling argument has been provided to

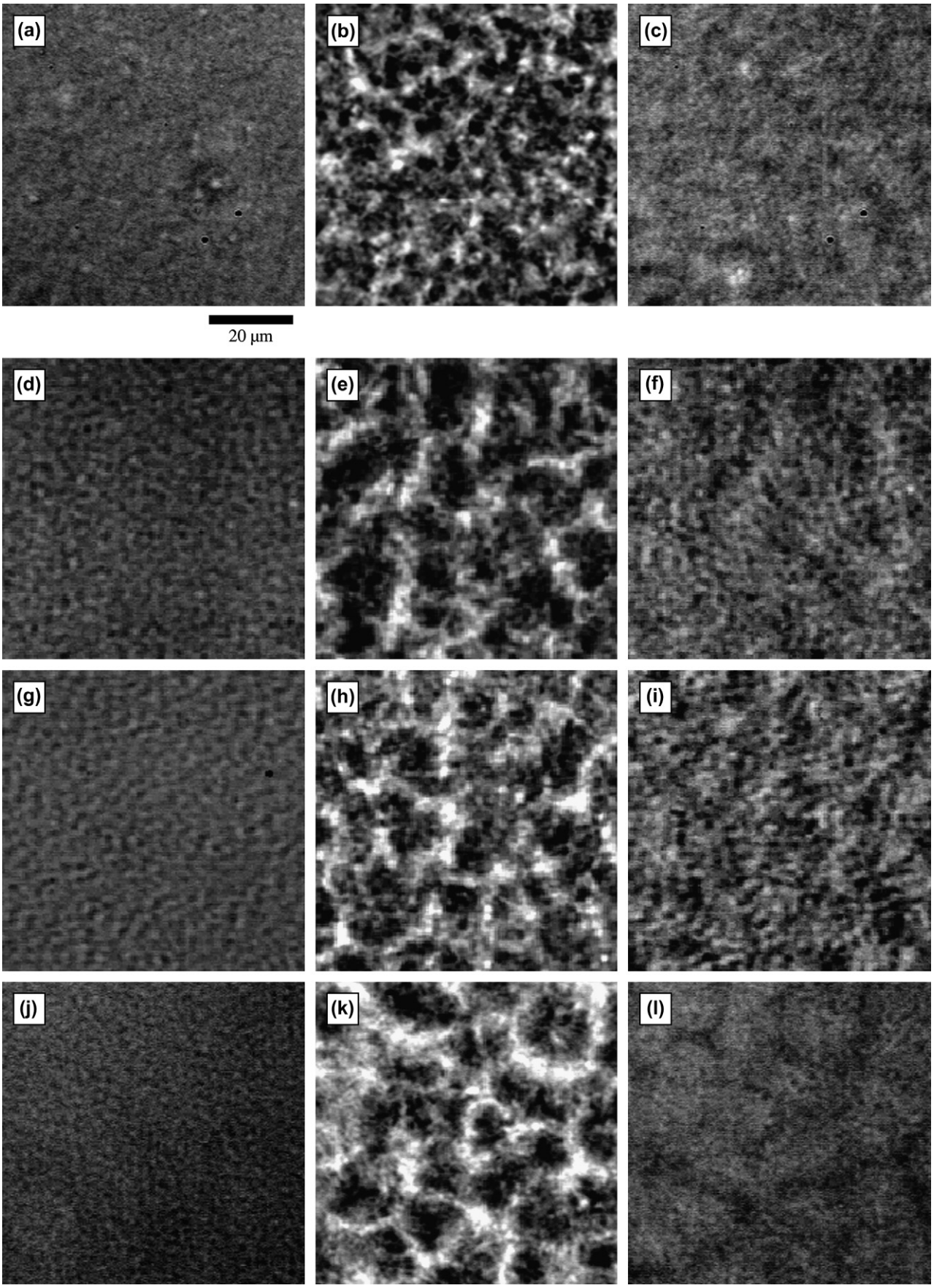

Fig. 9. Phase-contrast optical micrographs of H30 ((a) $t_{lps} = 246$ min, (b) $t_{cry,c4} = 346$ min, (c) $t_{lps,c4} = 357$ min), H40 ((d) $t_{lps} = 259$ min, (e) $t_{cry,c4} = 352$ min, (f) $t_{lps,c4} = 361$ min), H50 ((g) $t_{lps} = 247$ min, (h) $t_{cry,c4} = 331$ min, (i) $t_{lps,c4} = 337$ min) and H60 ((j) $t_{lps} = 234$ min, (k) $t_{cry,c4} = 315$ min, (l) $t_{lps,c4} = 318$ min). The scale bar at the bottom right of (a) is applicable for all images and represents 20 μm.

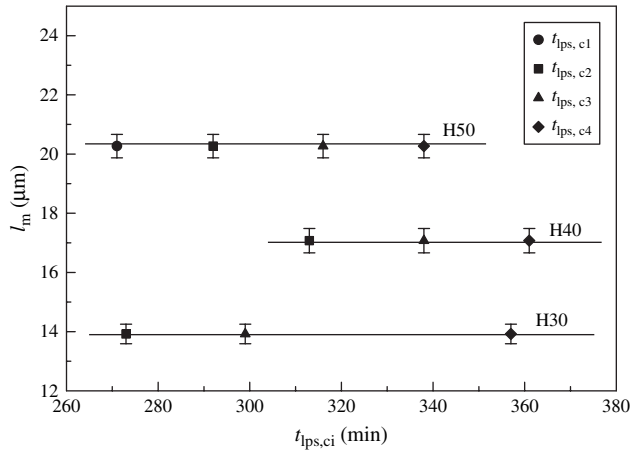

Fig. 10. Time dependence of the characteristic length, l_m for large secondary domain in H30, H40 and H50 at $T_{lps} = 130$ °C.

partially account for the observed phenomena. In CQ, characteristic lengths of secondary features induced by crystallization depend strongly on the overall PEH composition, whereas are insensitive to temperature cycling. The contrast of large domains becomes more prominent upon cyclic crystallization and remelting. On the other hand, primary LLPS domains coarsen with CQ while loosing the contrast.

Acknowledgement

The authors thank Dr. David J. Lohse (Exxon Mobil) for providing us the polymers used in this study. This study was supported by National Institute of Standards and Technology of the US Department of Commerce. HW acknowledges the support by the National Science Foundation (USA) under Grant No. 0348895. Z.G. Wang acknowledges the financial support from ''One Hundred Talents'' Program of Chinese Academy of Sciences and the National Science Foundation of China with grant numbers 10590355, 50573088 and 20674092.

References

[1] de Gennes PG. Scaling concepts in polymer physics. New York: Cornell University Press; 1979.
[2] Wunderlich B. Macromolecular physics. New York: Academic Press; 1973.
[3] Rhee J, Crist B. Macromolecules 1991;24(20):5663–9.
[4] Crist B, Hill MJ. J Polym Sci Part B Polym Phys 1997;35(14):2329–53.
[5] Keller A, Cheng SZD. Polymer 1998;39(19):4461–87.
[6] Inaba N, Sato K, Suzuki S, Hashimoto T. Macromolecules 1986;19(6): 1690–5.
[7] Inaba N, Yamada T, Suzuki S, Hashimoto T. Macromolecules 1988; 21(2):407–14.
[8] Tanaka H, Nishi T. Phys Rev Lett 1985;55(10):1102–5.
[9] Tanaka H, Nishi T. Phys Rev A 1989;39(2):783–94.
[10] Tanaka H, Yokokawa T, Abe H, Hayashi T, Nishi T. Phys Rev Lett 1990; 65(25):3136–9.
[11] Burghardt WR. Macromolecules 1989;22(5):2482–6.
[12] Wang H, Han CC. Abstr Pap Am Chem S 220: 466-POLY Part 2; August 20 2000.
[13] Wang H, Shimizu K, Hobbie EK, Wang ZG, Meredith JC, Karim A, et al. Macromolecules 2002;35(3):1072–8.
[14] Shimizu K, Wang H, Wang ZG, Matsuba G, Kim H, Han CC. Polymer 2004;45(21):7061–9.
[15] Shimizu K, Wang H, Wang ZG, Kim H, Han CC. Abstr Pap Am Chem S 223: 333-POLY Part 2; April 7 2002.
[16] Wang H, Shimizu K, Kim H, Hobbie EK, Wang ZG, Han CC. J Chem Phys 2002;116(16):7311–5.
[17] Shimizu K, Wang H, Wang ZG, Matsuba G, Han CC. Abstr Pap Am Chem S 224: 207-PMSE Part 2; August 18 2002.
[18] Han CC, Wang H, Shimizu K, Kim H, Hobbie EK, Wang ZG. Abstr Pap Am Chem S 224: 761-POLY Part 2; August 18 2002.
[19] Wang H, Wang GZG, Han CC, Hsiao BS. Abstr Pap Am Chem S 222: 255-PMSE Part 2; August 2001.
[20] Wang GZG, Wang H, Shimizu K, Han CC, Hsiao BS. Abstr Pap Am Chem S 222: 259-PMSE Part 2; August 2001.
[21] Wang ZG, Wang H, Shimizu K, Dong JY, Hsiao BS, Han CC. Polymer 2005;46(8):2675–84.
[22] Matsuba G, Shimizu K, Wang H, Wang ZG, Han CC. Abstr Pap Am Chem S 224: 206-PMSE Part 2; August 18 2002.
[23] Matsuba G, Shimizu K, Wang H, Wang ZG, Han CC. Proceedings of international symposium on polymer crystallization. Mishima, Japan; 2002. p. 198.
[24] Matsuba G, Shimizu K, Wang H, Wang ZG, Han CC. Polymer 2003; 44(24):7459–65.
[25] Matsuba G, Shimizu K, Wang H, Wang ZG, Han CC. Polymer 2004; 45(15):5137–44.
[26] Goldenfeld N. Lectures on phase transitions and the renormalization group. Advanced Book Program. Reading, MA: Addison-Wesley; 1992 [chapter 8].
[27] Zhang X, Wang Z, Muthukumar M, Han CC. Macromol Rapid Commun 2005;26(16):1285–8.
[28] Zhang X, Wang Z, Zhang R, Han CC. Macromolecules 2006;39(26): 9285–90.